PAPER • OPEN ACCESS

Experimental evaluation of signal-to-noise in spectro-holography via modified uniformly redundant arrays in the soft x-ray and extreme ultraviolet spectral regime

To cite this article: Christian M Günther *et al* 2017 *J. Opt.* **19** 064002

View the article online for updates and enhancements.

Related content

- High-resolution magnetic-domain imaging by Fourier transform holography at 21 nm wavelength
Stefan Schaffert, Bastian Pfau, Jan Geilhufe et al.

- Femtosecond pulse x-ray imaging with a large field of view
B Pfau, C M Günther, S Schaffert et al.

- Holographic imaging of interlayer coupling in Co/Pt/NiFe
Thomas A Duckworth, Feodor Y Ogrin, Guillaume Beutier et al.

Recent citations

- Achieving diffraction-limited resolution in soft-x-ray Fourier-transform holography
Jan Geilhufe et al

- Editorial for special issue on coherent diffractive imaging
H M Quiney et al

Experimental evaluation of signal-to-noise in spectro-holography via modified uniformly redundant arrays in the soft x-ray and extreme ultraviolet spectral regime

Christian M Günther[1], Erik Guehrs[1], Michael Schneider[2], Bastian Pfau[2], Clemens von Korff Schmising[2], Jan Geilhufe[2,3], Stefan Schaffert[1,4] and Stefan Eisebitt[1,2]

[1] Technische Universität Berlin, D-10623 Berlin, Germany
[2] Max-Born-Institut, D-12489, Berlin, Germany

E-mail: christian.guenther@tu-berlin.de (Christian Günther) and eisebitt@mbi-berlin.de (Stefan Eisebitt)

CrossMark

Abstract

We present dichroic x-ray lensless magnetic imaging by Fourier transform holography with an extended reference scheme via a modified uniformly redundant array (mURA). Holographic images of magnetic domains simultaneously generated by a single pinhole reference as well as by a mURA reference are compared with respect to the signal-to-noise ratio (SNR) as a function of exposure time. We apply this approach for spectro-holographic imaging of ferromagnetic domain patterns in Co/Pt multilayer films. Soft x-rays with wavelengths of 1.59 nm (Co L_3 absorption edge) and 20.8 nm (Co $M_{2,3}$ absorption edges) are used for image formation and to generate contrast via x-ray magnetic circular dichroism. For a given exposure time, the mURA-based holography allows to decouple the reconstruction SNR from the spatial resolution. For 1.59 nm wavelength, the reconstruction via the extended reference scheme shows no significant loss of spatial resolution compared to the single pinhole reference. In contrast, at 20.8 nm wavelength the single pinhole reveals some very intricate features which are lost in the image generated by the mURA, although overall a high-quality image is generated. The SNR-advantage of the mURA scheme is most notable when the hologram has to be encoded with few photons, while errors associated with the increased complexity of the reconstruction process reduce the advantage for high-photon-number experiments.

Keywords: magnetic circular dichroism, imaging and optical processing, holography, x-ray imaging, diffraction efficiency, resolution and other hologram characteristics, magnetic domains in thin films

(Some figures may appear in colour only in the online journal)

---

[3] Present address: Canadian Light Source, SK S7N 2V3, Saskatoon, Canada.
[4] Present address: Siemens Healthcare GmbH, 91052 Erlangen, Germany.

1. Introduction

Fourier transform holography (FTH) is an imaging technique that is based on the interference of the light scattered by an object with a spherical reference wave originating in or close to the object plane [1]. With the appreciable coherent photon flux from 3rd generation synchrotrons as well as the increased availability of free-electron x-ray lasers on one hand and

laser-driven high harmonic generation (HHG) sources on the other hand, FTH has become possible over a large spectral range, including the extreme ultraviolet (XUV), the soft x-ray regime and even hard x-rays [1–3]. With the advent of 4th generation storage rings that will be diffraction-limited sources of x-rays well beyond 1 keV photon energy, interference-based imaging can be expected to gain further importance, similarly to its use at free-electron x-ray lasers [4–8]. For laboratory sources, extending the wavelength range towards such short wavelengths with coherent photon fluxes suitable for high-resolution imaging is still a formidable challenge, but progress in recent years has been fast [9–14]. Nevertheless, while FTH with x-rays has become routine at 3rd generation synchrotron sources [1, 15–20], when pushing the resolution below the 10 nm region, investigating very weak contrast objects, imaging with extreme temporal resolution or even via a single femtosecond flash exposure at short wavelengths, the signal-to-noise ratio (SNR) achievable in the hologram at high momentum transfer remains a challenge.

In mask-based FTH, a spherical reference wave is created by a single reference aperture in the object plane [1, 2]. The image is generated by a two-dimensional Fourier transform, where the achievable spatial resolution is limited by the lateral dimension of this pinhole as well as the maximum momentum transfer signal recorded. As a consequence, a tradeoff exists between spatial resolution and contrast of the generated image, as the intensity of the reference wave modulating the hologram at high momentum transfer is typically the limiting factor. This is the limit we consider in this work. A direct way to improve the signal-to-noise ratio is reference multiplexing, the generation of multiple *independent* images by multiple references at suitable locations [4, 21]. Here, the 'real estate' available for image reconstructions that can be added up is connected to the size of the Fourier transformed hologram, the so called Patterson map and, together with the pixel resolution, limited by the detector pixel array [1]. Extended reference approaches allow to overcome the tradeoff between intensity and resolution by collecting more photons to contribute to the reference signal, while at the same time providing a sharp point spread function and, thus, conserving the high spatial resolution. In principle, very general structures may be used to provide a reference signal [22]. For a known shape of the reference aperture its contribution can be removed from the cross-correlation term with the object, yielding an image of the object. However, for certain special reference schemes it is possible to obtain an image in a more direct way without the necessity of an iterative reconstruction algorithm. Representatives of such schemes with the goal to increase reference wave intensity are uniformly redundant arrays (URAs) [23] and Fresnel Zone plates [24]. The reconstruction is obtained by operators based on convolution or propagation.

In this work, we consider the SNR in magnetization imaging by a modified URA (mURA) [23, 25, 26]. An additional single pinhole is used to obtain an independent FTH image in the exact same measurement, allowing to compare the respective SNR. We image the nanoscale domain pattern of perpendicular magnetic anisotropy samples via x-ray magnetic circular dichroism (XMCD) [2, 27]. We compare the magnetization contrast in images that are generated from the difference of two holograms recorded with opposite helicities with images from a single helicity. The latter case is especially important for destructive single-shot measurements at XFEL sources. Finally, we demonstrate the use of mURAs for magnetic imaging not only for one of the widely used *L*-edges of 3d transition metal compounds, but also for the *M*-edges in the XUV range, where magnetic circular dichroism has recently been shown to be accessible with HHG lab sources [28].

2. Methods

2.1. Holography geometry and magnetic sample composition

Resonant soft x-ray holography was carried out in Fourier transform geometry, realized via a micro/nano-structured mask integrated with the sample as introduced by Eisebitt *et al* [2]. On a silicon nitride (Si_3N_4) membrane an optical mask is defined on one side and the specimen to be imaged is rigidly attached on the opposite surface of the membrane [29]. In our case the specimen to be imaged is the projected 2D magnetization distribution within a thin metallic multilayer film with perpendicular magnetic anisotropy. The parameters of the three components—substrate, mask and magnetic layer—are optimized for the scattering experiments at the very different wavelengths in the XUV ($\lambda = 20.8$ nm, $\hbar\omega = 59.6$ eV) and soft x-ray ($\lambda = 1.59$ nm, $\hbar\omega = 778$ eV) regime. The exact wavelengths used are determined by the ability to generate magnetic contrast via XMCD at the corresponding Co $M_{2,3}$ and L_3 absorption edges [30, 31]. At both edges, holograms with opposite circular helicity of the incoming soft x-rays are recorded.

For *L*-edge imaging the thicknesses of the Si_3N_4 membrane and the Au layer fabricated by thermal evaporation are 100 nm and 1 μm, respectively. The latter is used to define the holography geometry by focused-ion-beam milling. A circular object aperture of 2 μm diameter is defined in the Au-layer only. Laterally offset from the circular object mask, a single pinhole and a mURA are defined as structures each providing independent reference beams [21], as shown in the main panel of figure 1. These reference apertures penetrate the complete sample structure, including the magnetic thin film. Since the aspect ratio is a limiting factor for the focused-ion-beam generation of such structures, the magnetic layer was removed locally to ensure that pinholes with apex diameters below 50 nm could be fabricated. The diameter of the pinholes again is a resolution-limiting factor in single-pinhole or mURA FTH. The advantage of the mURA lies in faster data acquisition as each individual pinhole generates an independent signal that will add in the final decoded image. Upper boundaries on the size of the mURA are set on one hand by the associated required increase of the object-mURA distance, which is limited by the coherence length of the light as well as the *q*-sampling parameters of the detector. On the other hand, a strong imbalance of the signal strengths originating from
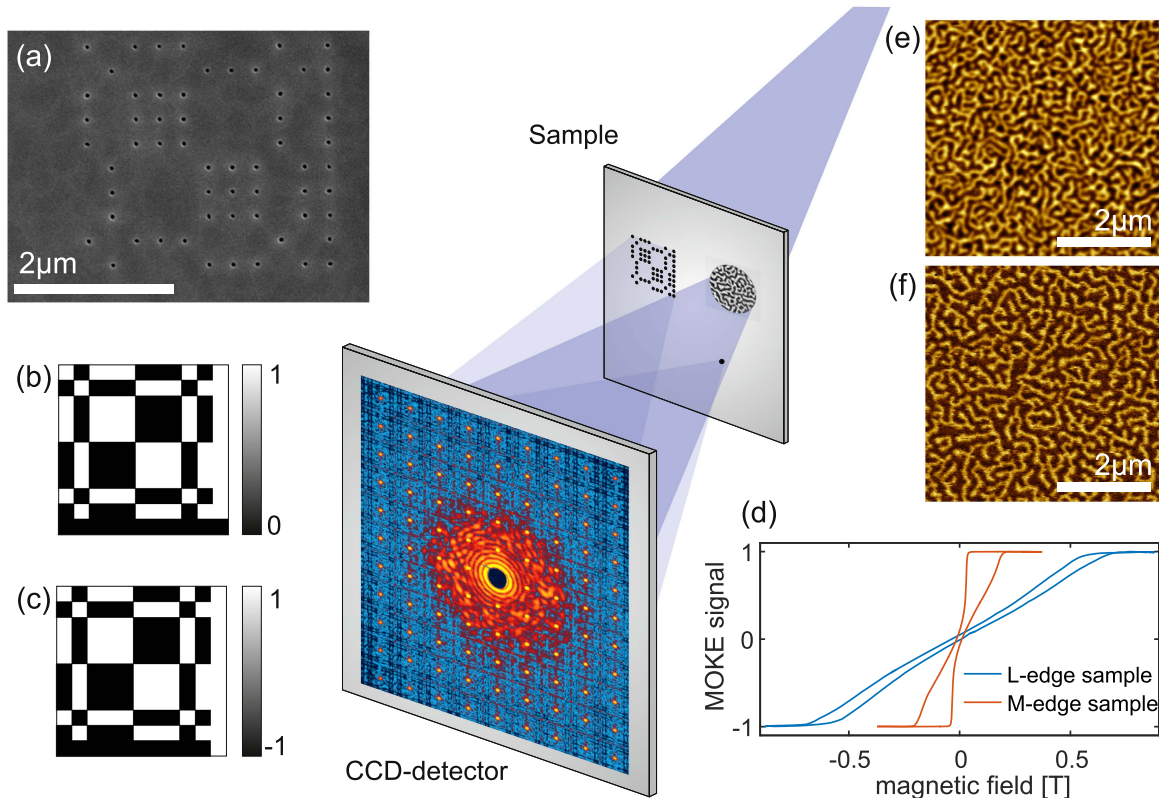
Figure 1. General FTH setup (a) SEM image of the pinhole array representing the (b) theoretical mURA. (c) Corresponding decoding pattern for (b). Characterization of the magnetic properties of the thin films by (d) out-of-plane MOKE measurements and $5 \times 5 \ \mu m^2$ MFM-images of the domain pattern for the samples used for (e) *L*- and (f) *M*-edge imaging.

object and reference results in reduced contrast in the final image.

Here, the experimental realization of the mURA shown in figure 1(a) consists of 60 transmissive pinholes on a square grid with 300 nm pitch, similar to some of the structures used by Marchesini *et al* [23], but with individual apertures about a factor of two smaller. The theoretical layout of the mURA featuring 11×11 elements and the corresponding decoding pattern are visualized in panels (b) and (c) of figure 1 [25, 26]. Note that the decoding pattern has a value range of $[-1, +1]$, while the mURA is defined by a transmission function ranging from zero to unity. Deviations from the theoretical pattern, e.g. variations in position, shape and size of the individual pinholes result in imperfect decoding and thus contribute additional noise to the decoded image which is discussed in the results section.

A Co/Pt multilayer film of 100 nm thickness, with composition $Pt(30 \text{ Å})/[Co(12 \text{ Å})/Pt(7 \text{ Å})]_{50}/Pt(13 \text{ Å})$, was fabricated by magnetron sputter deposition onto the Si_3N_4 membrane. Pt(30 Å) serves as growth buffer layer, while the top Pt(13 Å) layer prevents oxidation. The corresponding hysteresis loop measured by polar magneto-optical Kerr effect (MOKE) indicates perpendicular magnetic anisotropy (figure 1(d)) which is typical for such multilayer systems [32]. Demagnetization along the sample normal generates a labyrinth domain pattern with alternatingly up and down magnetized domains as observed in the magnetic force microscopy (MFM) image in figure 1(e).

For *M*-edge imaging the thickness of the Si_3N_4 substrate is reduced to 30 nm in order to minimize the substrate absorption at 59.6 eV photon energy, where one attenuation length is only 50 nm. At this photon energy, a $[Cr(5 \text{ nm})/Au (50 \text{ nm})]_5$ multilayer with 300 nm overall thickness is sufficient as an opaque mask to define the holography geometry, which laterally is similar to the one of the *L*-edge sample. The diameter of the object aperture is again 2 μm, the size of the reference pinhole and the mURA pinholes was set to yield apertures below 65 nm diameter. Due to an astigmatism of the ion beam the final pinholes exhibit an oval shape with axes of 65 nm and 80 nm length. The composition of the magnetic thin film is $Ta(20 \text{ Å})/Pt(30 \text{ Å})/[Co(8 \text{ Å})/Pt(14 \text{ Å})]_{11}/Pt(6 \text{ Å})$ resulting in a thin film of 30 nm overall thickness. The MOKE hysteresis loop and a MFM image revealing the typical labyrinth pattern of out-of-plane domains are shown in figures 1(d) and (f), respectively.

2.2. Experimental setup

The x-ray experiments were performed at the BESSY-II synchrotron source in Berlin, Germany. A schematic of the general FTH layout is shown in the main panel of figure 1. The diffraction pattern generated upon coherent illumination of the sample described above is recorded by a $27.6 \times 27.6 \ mm^2$ (2048 pixels × 2048 pixels) in-vacuum, back-illuminated charge-coupled device (CCD) camera (Princeton Instruments PI-MTE). Co *L*- and *M*-edge imaging
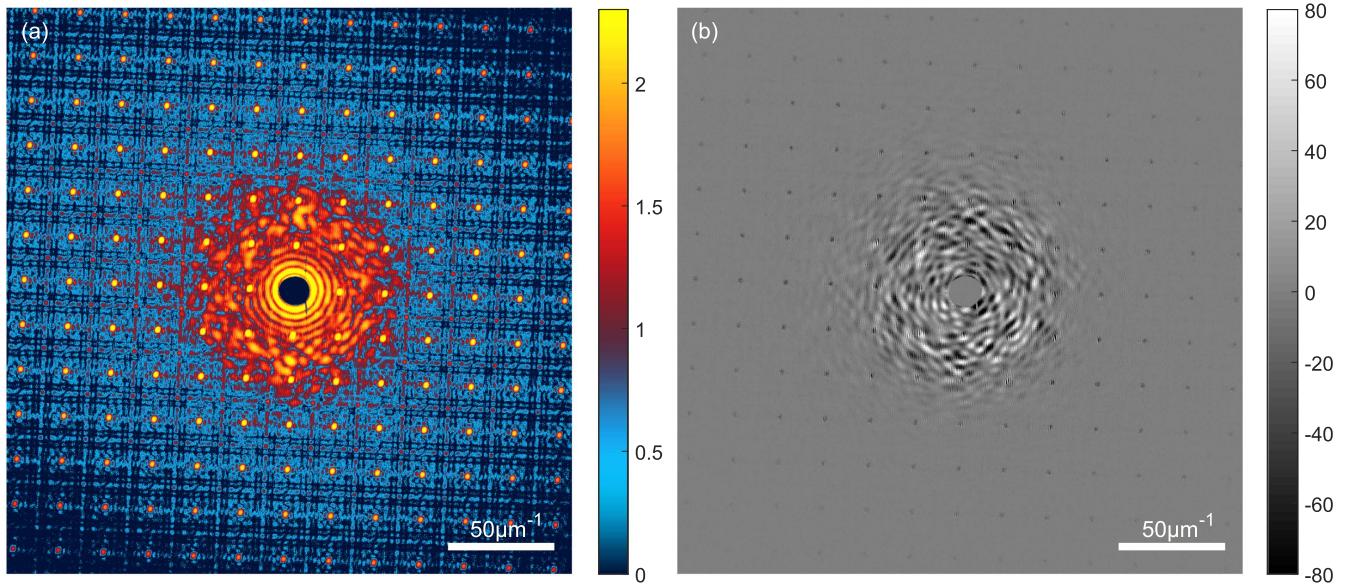
Figure 2. (a) Hologram recorded with positive helicity accumulated for 15×60 s. The pseudocolor intensity scale corresponds to the logarithm of the number of detected photons. (b) Difference of two holograms (each 15 x 60 s) recorded with opposite helicities on linear intensity scale. In both panels the full detector image (2048×2048 pixels) is shown.

Table 1. Summary of the experimental parameters at the two BESSY-II beamlines [33].

	UE56/2-PGM-1	UE112-PGM1
energy (eV)	778	59.6
energy resolution (eV)	0.880	0.027
flux (ph/(s 0.1% bandwidth))	4×10^{13}	4×10^{13}
divergence (horz.$\times$vert.) (mrad)	10×10	1.4×0.6
focus–sample distance (cm)	28	11
sample–detector distance (cm)	41	4.1
detectable momentum transfer q_{max} (μm^{-1})	266	204
diffraction-limited resolution (nm)	48	65

was performed at the UE56/2-PGM-1 and UE112-PGM1 beamlines, respectively. The experimental parameters for both beamlines are given in table 1 [33]. The maximum XMCD contrast was determined by measuring the energy-dependent transmission through a magnetically saturated cobalt reference sample as function of the helicity of the incident radiation. A circular beamstop of about 1 mm diameter mounted in front of the CCD camera blocked the intense direct beam to account for the limited dynamic range of the CCD.

For *L*-edge imaging the strong spatial filtering caused by the high focus–sample distance was dictated by vacuum chamber constraints. The coherence of the beamline was determined by recording the scattering of a known aperture array and comparing it to the pattern predicted by theory for fully coherent illumination. Lower bounds for the horizontal and vertical coherence lengths of 3.3 μm and 4.2 μm were obtained, respectively [34].

For measurements at the Co *M*-edge a 200 nm Al filter upstream of the sample was used to reduce the third harmonic radiation residually present from the undulator. Given a maximum scattering angle of 18° from center to edge of the CCD chip, the small-angle approximation is not valid and the recorded hologram needs to be corrected for Ewald sphere curvature as well as for refraction effects [35]. An additional guard aperture with approximately 1.5 mm diameter against diffuse stray light bypassing the sample holder was placed directly downstream of the sample.

3. Results

3.1. Hologram reconstruction and mURA decoding

At the Co *L*-edge a set of 15 separate frames each with 60 s exposure time was recorded for both helicities. After dark field subtraction, each frame was normalized to denote the number of detected photons. In figure 2(a) the decadic logarithm of the sum of all 15 frames with positive helicity is shown on a pseudocolor intensity scale. The central part close to zero momentum transfer is blocked by the beamstop. Adjacent, pronounced Airy fringes generated by the circular object aperture are evident. In the momentum transfer range of about $q = 25 \, \mu m^{-1}$ to $50 \, \mu m^{-1}$ the resonant scattering caused by the presence of magnetic domains [36] is strongly visible. These values translate to a domain periodicity of 125–250 nm. The prominent lattice of Bragg peaks is generated by the mURA. The brightest spots are separated by a Δq of 21 μm^{-1} corresponding to the smallest distance between neighboring elements of the mURA of 300 nm. Note that these intense peaks—which will get more pronounced for larger URAs—can present a problem if detectors with a limited dynamic range such as our CCD are used. Once the
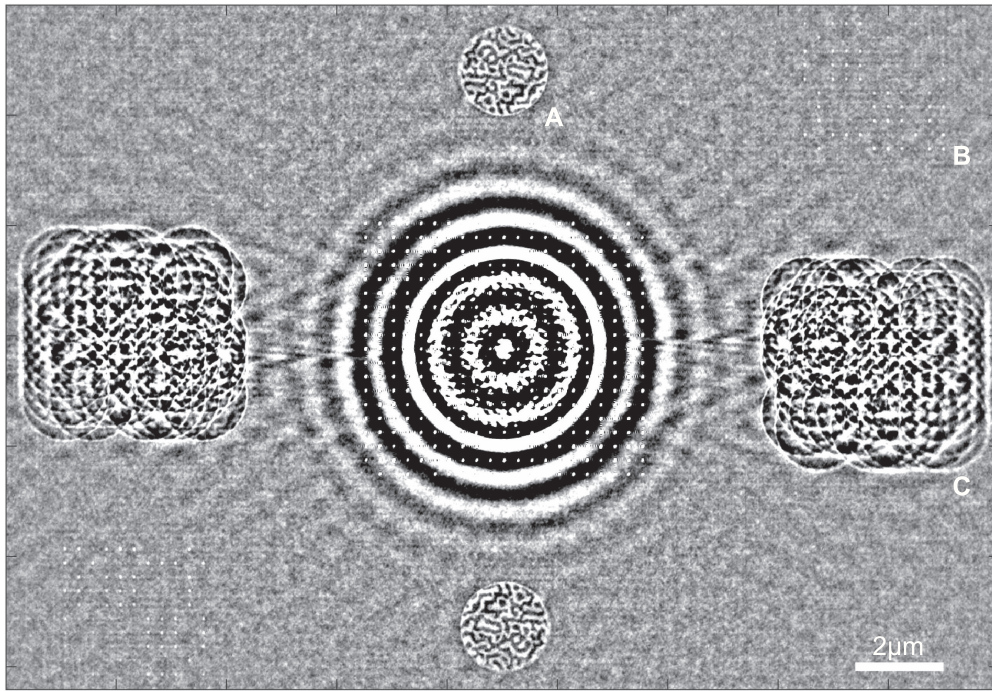
Figure 3. Center region (45% × 30%) of the real part of the 2D-Fourier transform of the hologram visualized in figure 2(a). The linear intensity scale was adjusted for good visibility of the three cross-correlation images generated between pinhole, mURA and object.

Bragg peak intensities reach values limiting a weaker sample scattering being detected due to the given dynamic range, one would like to attenuate these beams similar to the $q = 0$ beam, which is obviously a difficult task. Figure 2(b) shows the difference of two holograms recorded with positive and negative helicities (15 frames each) on linear intensity scale. Here the non-magnetic charge part of the scattering cancels out to first order in the subtraction and, thus, the magnetic part of the scattering signal is enhanced. As a consequence, one can directly observe weak magnetic scattering up to $q = 100 \, \mu\mathrm{m}^{-1}$.

In figure 3 the central part of the Patterson map obtained by a two-dimensional Fourier transform of the positive helicity hologram visualized in figure 2(a) is presented. Numerical treatment of the hologram included $q = 0$ centering, cosmic ray removal and smoothing the abrupt intensity changes at the beamstop edges to reduce FFT artifacts as well as an interpolation of the final Patterson map to half the pixel size.

Beams through all transmissive areas of the holography mask are able to interfere and generate respective cross-terms in the Patterson map. The center contains the autocorrelation of all transmissive areas and it is surrounded by strong ringing artifacts due to the beamstop, which damp out towards the cross-correlation areas of the Patterson map. The three cross-correlation pair 'images' of object, mURA and single pinhole aperture form at locations defined by the connecting vector of the specific two apertures [1]. In detail these are the cross-correlations of: *pinhole & object* forming above and below the center at position marked 'A'. This term corresponds to standard mask-based FTH and directly provides an image of the magnetic domain state within the object aperture defining

the field of view (FOV). *Pinhole & mURA* cross-correlations are located in the lower left and upper right corner, labeled 'B'. Here, the single pinhole directly images the transmission of the mURA pinhole array. In that way, the actual transmission through the individual mURA pinholes can be directly measured in the very same experiment used to image the object. Note that this at-wavelength measurement of the transmission and exact location of each source point within the mURA is much superior to SEM images of the reference object and can be used to correct mURA imperfections to obtain higher resolution, as is generally true with knowledge of extended references [22]. One could thus use a single high-resolution aperture to characterize a larger reference structure such as the mURA to combine highest spatial resolution with optimized reconstruction intensity. While this would require a two-step, but non-iterative analysis, the data could be acquired in a single exposure. This analysis is beyond the scope of this paper; here we restrict ourselves to determining the exact mURA orientation (2.3°) and pixel-pitch (25.1 pixel) from this measurement, as these parameters are required for decoding the cross-correlation of the object and the mURA reference. The diameter of single spots in this image of the mURA is 50 nm. Note that this value results from the cross-correlation of two (nominal) identical pinholes. Thus, assuming a Gaussian shape for the transmission of the individual apertures, their transmission FWHM is a factor of $\sqrt{2}$ smaller. Finally, the *mURA & object* cross-correlation term is clearly visible in the Patterson map in figure 3 at 'C'. This cross-correlation term constitutes the superposition of the 60 images each generated by one of the 60 open elements of the mURA, analogous to the isolated pinhole, and as previously demonstrated by Marchesini *et al*

[23]. Since the intermediate distance between the mURA pinholes is smaller than the object size, these images are overlapping. Note that for larger mURAs containing more pinhole apertures the mURA & object cross-correlation term grows accordingly and requires an increased distance between both apertures to avoid overlap. The maximum distance between the apertures is limited by the coherence length and the pixel number of the detector [5].

The FTH image (A) and the mURA-object cross-correlation (C) are cropped for further processing. For both, the contrast is maximized into the real part by complex rotation as the analysis of the spatial domain distribution rather than an absorption versus phase contrast analysis is the typical imaging goal for this kind of sample.

An image from the mURA & object cross-correlation is obtained by convolution with the 2×2 tiled decoding pattern (figure 1(c)) matched to the pixel distance of the mURA in the reconstruction. Note that for the scaled decoding pattern the individual $2 \times 2 \times 11^2$ elements represented by single pixels with values of ± 1 are separated by large areas of zeros which are omitted in figure 1(c). For clarity, in figure 3 we have demonstrated the contributions to the Patterson map using a single-helicity measurement. It is clear that with sufficient SNR such as obtained from the hologram in figure 2(a) domain images can easily be obtained with one helicity only [4, 35]. This is of particular relevance for destructive single-shot experiments, e.g., at free-electron x-ray lasers. Now we will continue the discussion with standard helicity difference holograms, which allow to suppress non-magnetic contributions [1, 16, 17].

3.2. Evaluation of the signal-to-noise ratio

The hologram reconstruction process as described in the previous section produces two independent images of the sample's nanoscale magnetic domain pattern, one originating from the single pinhole reference and the other from the mURA. These two images generated from the Co *L*-edge helicity difference hologram shown in figure 2(b) are compared in figures 4(a) and (b), respectively. Both, the single pinhole and the mURA provide almost identical reconstructions allowing to unambiguously identify the arrangement of the up/down oriented ferromagnetic domains in the multilayer film. Only very slight differences can be found, for example looking at the bubble-like domain indicated by the green arrow, illustrating the high level of confidence in the structure obtained. A reason for these minute deviations might be imperfect matching of the decoding pattern to the experimental data. Line profiles (figure 4(e)) crossing domain borders at the indicated locations confirm a spatial resolution of approximately 50 nm for both images, as defined by the 10%–90% criterion. Note that this is a conservative estimate as the domain wall itself can have a sizeable width, depending on multilayer composition and thickness [37]. That value fits well with the recorded momentum transfer of $q = 266 \, \mu m^{-1}$ which translates to a spatial resolution of 48 nm and is corroborated by the diameter of 50 nm of single spots in the pinhole/mURA cross-correlation term. As the hologram
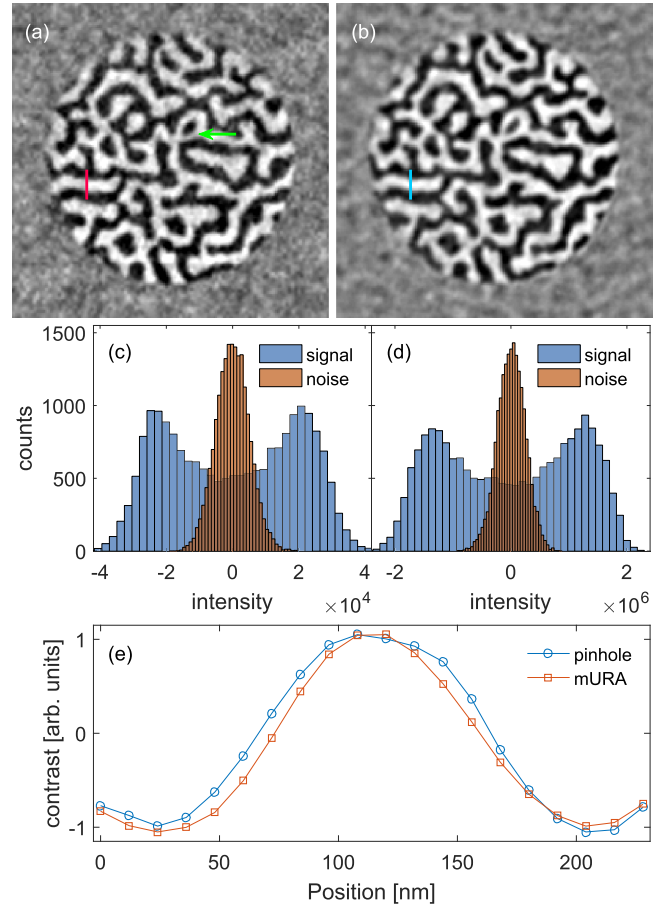

Figure 4. The magnetic domain patterns reconstructed from the helicity-difference hologram in figure 2(b) generated by (a) the FTH pinhole and (b) the mURA. The contrast is scaled to 1%–99% and the circular FOV is 2 μm in diameter. Histograms of the FOV (signal) and the surrounding area (noise) are visualized in (c) for the FTH and (d) the mURA image. Bins correspond to the intensity values in the reconstructions. (e) Normalized line profiles as indicated in panels (a) and (b).

leading to the reconstructions in figure 4 is recorded with 1800 s overall exposure time and correspondingly high SNR, a significant advantage of the mURA hologram over the standard single pinhole reference version is not to be expected.

Our samples would in an ideal case result in a bimodal intensity histogram due to the dominance of magnetic domains either being fully magnetized up or down, i.e., appearing black or white, with only smaller fractions of the FOV being in intermediate states at the domain walls and thus represented as shades of gray [37]. We therefore quantify the SNR in the reconstructed images by analysis of the image contrast. In figures 4(c) and (d) histograms featuring 40 bins generated from panels (a) and (b) visualize the contrast distribution within the circular FOV (signal) and the surrounding area (noise).

The latter region should in an ideal case be at a constant intermediate gray level, as no signal from this masked area contributes to the hologram. Intensity fluctuations in this region of the reconstruction are thus indicative of systematic errors, and the ratio of the two variance values within and
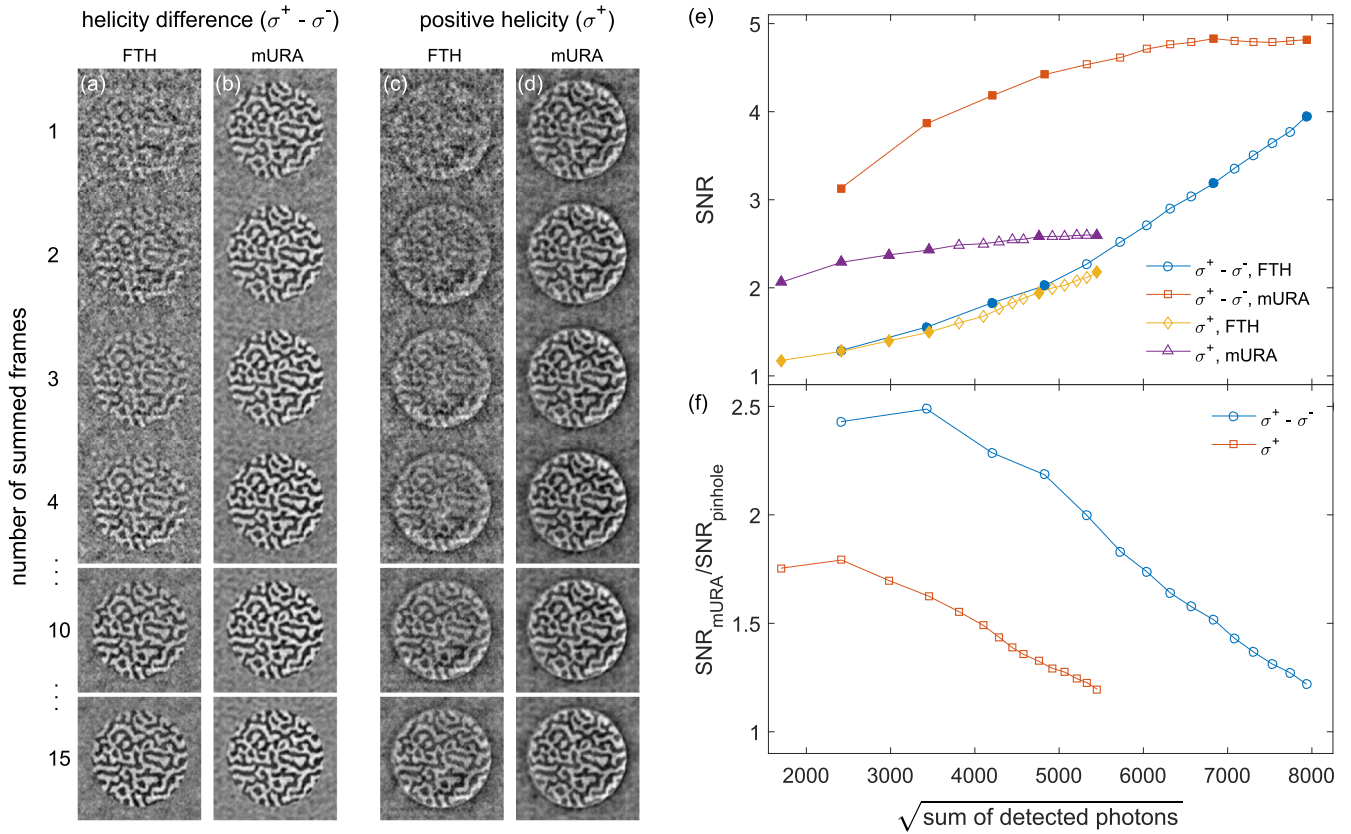
Figure 5. Domain patterns generated from helicity-difference holograms (compare figure 2(b)) with exposure times of 120 s per frame number generated by (a) the single pinhole and (b) the mURA. (c) Single pinhole and (d) mURA generated images from positive helicity alone (compare figure 2(a)). Here, the exposure time is 60 s per frame number. (e) SNR derived from panels (a)–(d), filled markers correspond to images shown. (f) $SNR_{mURA}/SNR_{pinhole}$ for images recorded from helicity differences and positive helicity only.

outside the FOV can be used to quantify how much stronger real variations in the image contrast are detectable over artificial fluctuations which are seen outside the FOV and can be expected to exist within the FOV at the same level. For the pinhole- and mURA-generated images the signal exhibits two peaks distributed symmetrically around zero generated by the black and white domains. The noise follows a Gaussian distribution around zero. We approximate the widths of these histogram curves, which is proportional to the contrast, with the square root of the variance, i.e., the standard deviation, of the contributing image part. Finally, we denote the ratio of these two standard deviations inside and outside of the FOV as SNR of the image. For figures 4(a) and (b) we obtain values of $SNR_{pinhole} = 3.9$ and $SNR_{mURA} = 4.8$, respectively.

To investigate the SNR advantage of a mURA hologram when an image has to be formed with less incident photons, the separately recorded frames each with 60 s exposure time of the hologram are used to illustrate how the contrast builds up in the image series. The reconstructions shown in figures 5(a)–(d) consider only the scattered photons detected up to frame numbers of 1 to 4, 10 and 15. Photons detected in the immediate vicinity of the beamstop shadow were excluded up to the same momentum transfer boundary for each hologram, in order to avoid any systematic errors associated with a potential shift of the beamstop relative to the

diffraction pattern. In panels (a) and (b) helicity difference reconstructions are shown, while panels (c) and (d) correspond to reconstructions from single-helicity holograms alone. For both cases the images generated by the single pinhole ((a) and (c)) and the mURA ((b) and (d)) are presented.

Inspection of the noise and contrast in the reconstructed images clearly shows that for lower total exposure time better images are obtained for the mURA reference compared to the pinhole reference, and that helicity difference images are superior to single helicity reconstructions. As can be expected, for very high total exposure resulting in high SNR in the holograms, these differences become less pronounced. As detailed before, we calculate the SNRs for each of the 15 frames within the exposure series. The corresponding plots of the SNR are shown in figure 5(e). The SNR values are plotted over the square root of the detected photon number (rather than over the square root of the exposure time) to compensate for varying sample illumination caused by a slow drift of the x-ray beam that was observed during the recording of the exposure series. Note that scaling the x-axis with the square root of detected photons introduces a non-linearity for the growth of the detector's readout noise which increases linearly with the square root of the number of exposures.

In *in-line* holography, only photons that have passed the first pinhole aperture contribute to the scattering from the

object to be imaged. The intensities of object and reference beam are thus not entirely independent. In this case the SNR was found to scale with the square of the number of photons that are incident on the object [38], in accordance with what one may expect from Poisson photon statistics. Similarly, for a given intensity balance between reference and object wave (which is of course subject to change for imaging the same object with different reference structures such as a single pinhole and a mURA), the same quadratic dependence is expected in FTH [23].

In the SNR estimate plots in figure 5(e) we observe the trend that for single-pinhole-based FTH the SNR grows with the square root of the number of accumulated photons, with helicity-difference holograms providing substantially increased SNR for a given photon number. A small deviation from this linear behavior is observed, caused by the drift of the illumination discussed above. In contrast, the SNR for the mURA deviates from this Poisson statistics behavior, with comparatively lower SNR increase at higher exposures. We attribute this to systematic contributions to the background noise in the images generated via the mURA reference. Note the different character of intensity fluctuations outside the FOV in the reconstructions in figures 4(a), (b) for the different reference schemes. In this area, which should appear flat, an increase of fluctuations with a spatial correlation length similar to the in-plane domain correlation length is observed in the mURA reconstruction in (b), but not in the single pinhole reconstruction in (a). We suspect the cause to be imperfect matching of the mURA decoding pattern to the real spatial distribution of the mURA transmission function. As a result, there is a component in the background noise that scales with the signal from the object. Consequently, the SNR for the mURA tends to grow slower than the square root of the exposure for high exposure times. On the other hand, the substantial SNR advantage of the mURA reconstructions over the single pinhole FTH for lower photon numbers is evident from the data compiled in figure 5.

To directly compare the SNRs of mURA and pinhole, their ratio $SNR_{mURA}/SNR_{pinhole}$ is plotted in figure 5(f). For low photon numbers, the mURA provides a 1.5 times higher SNR than the pinhole for a single difference image and the factor rises to 2.5 for a magnetization map obtained from a helicity difference hologram. According to Marchesini *et al* [23] for an URA with n open elements the SNR scales with:

$$SNR_n = \frac{SNR_1 \sqrt{n}}{2\sqrt{2}}$$

resulting in $SNR_{60}/SNR_1 = 2.7$ which is in reasonable agreement with our observations for difference-helicity imaging in the low-photon limit, where the counting statistics of photons detected in the hologram is expected to be the dominant limiting factor. We suspect that the reduced SNR gain in the case of single-helicity holography is due to artifacts that originate from non-magnetic contributions. These include ringing of the Fourier transform at steep intensity edges and affect the background SNR. Such contributions are usually eliminated in reconstructions from difference holograms. A detailed understanding of this finding will have to

await numerical modeling, which is beyond the scope of this article. The less important photon counting statistics does become a dominant source of noise, the more the SNR ratio decreases. This is the case for increasingly higher exposure times for both single and difference helicity reconstructions for the reasons discussed above. Under high-dose conditions where the incident coherent photon flux is not a limiting factor, the efficiency gain of holographic encoding via more complex high-intensity references such as a URAs or FZPs [24] is thus limited, while the complexity of experiment and the potential for systematic errors introduced, e.g., via imperfect knowledge of the URA, is increased. Vice versa, the efficiency advantage is obviously relevant when the available coherent photon flux is limited, as will be encountered for many experiments in single-shot experiments or when using table-top sources.

We would like to point out that the analysis presented here, based on a multiplexed experiment containing a single pinhole and a mURA reference at the same time, neglects any cross-talk effects of the two holograms recorded on the same detector within the same exposures. These depend on several experimental factors including the coherence of the illumination and the dynamic range of the detector.

3.3. mURA spectro-holography at the Co M-edge

While XMCD is a very strong contrast mechanism at the 3d transition metal *L*-edges with asymmetries, e.g., exceeding 20% for iron and cobalt [31], much weaker contrast on the order of only 1% is available at the respective *M*-edges. At the same time, the formation of a high-resolution image is more challenging given that the wavelength of the radiation employed is more than a factor of ten larger compared to the L_3 resonances of these elements. Nevertheless, spectro-holographic imaging at these wavelength is of large interest for sub-picosecond time-resolved studies, as this spectral range can currently be reached by the soft-x-ray free-electron lasers FLASH [5, 7, 39] and FERMI [8] and has become increasingly accessible with sufficient coherent photon flux via the rapidly developing laser-based laboratory sources exploiting HHG [13, 14, 28]. Imaging with XMCD contrast in the XUV spectral range is thus an interesting test case for mURA-based spectro-holography.

With a suitably designed sample as described above, we have carried out a FTH experiment again based on a multiplexed measurement containing both a single aperture and a mURA reference structure. A single dataset consisting of two holograms with opposite helicity and an exposure time of 150 s each was recorded. The helicity-difference hologram and the resulting reconstructions are presented in figure 6.

Focusing on the Bragg peaks in figure 6(a) generated by the mURA it becomes evident that their regular spacing is mapped with increasing distortion for increasing momentum transfer. This is a direct consequence of the large scattering angle up to 18° and the resulting mapping of the strongly curved Ewald sphere on the flat 2D detector. The appropriate corrections to obtain high-quality images have been discussed elsewhere [35] and are applied here, together with a
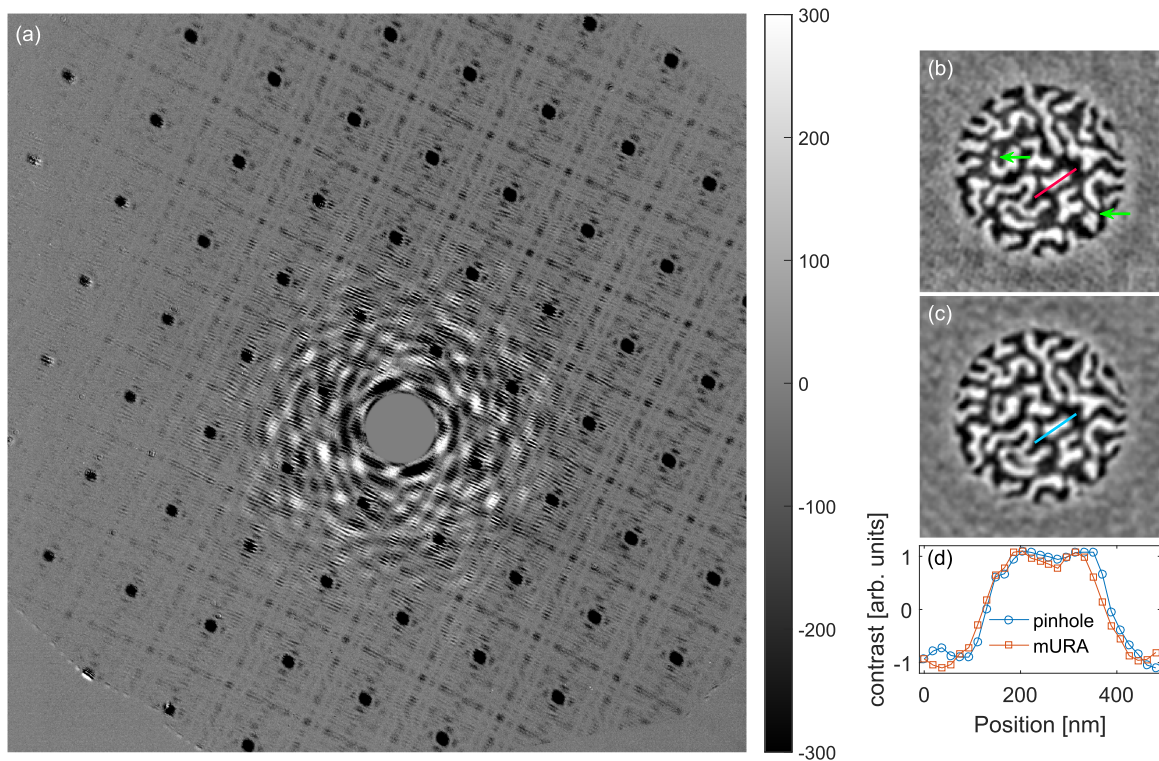
Figure 6. (a) Unprojected helicity difference hologram with *z*-scale ranging from −300 to 300 analog-to-digital units (ADUs). The distance between two neighboring Bragg peaks corresponds to 21 μm⁻¹. (b) Pinhole and (c) mURA reconstruction with contrast scaled to 1% to 99% obtained from (a) plus their corresponding normalized line profiles shown in (d). The FOV corresponds to 2 μm.

Blackmann-Harris window function to reduce FFT artifacts originating from a guard aperture behind the sample creating a sharp cut-off at the high scattering angles. Again, the mURA pitch and rotation can be determined from the at-wavelength transmission of the mURA as mapped via the cross-correlation with the single pinhole reference. The diameter of single spots in this cross-correlation corresponds to 90 nm.

The resulting pinhole and mURA reconstructions are shown in figures 6(b) and (c), respectively. In these images, after zeropadding, one pixel corresponds to 19 nm. As in the case of *L*-edge holography, in general the domain patterns seen in the reconstructions agree very well. A line profile crossing domain walls indicates a spatial resolution of about 90 nm, as defined by the 10%–90% criterion. Again, note that this is a conservative estimate due to the existence of a magnetization transition region in the domain wall [37]. However, the pinhole image reveals small domains which are lost in the mURA reconstruction, examples are marked by the green arrows. These small features appear 'smeared over' with intermediate contrast corresponding to unphysical 'intermediate magnetization' at positions in the labyrinth domain pattern where a full remanent magnetization can be expected. Apparently, the overall spatial resolution of the single pinhole is thus higher compared to the mURA. We attribute this finding to inhomogeneities of the 60 pinholes forming the mURA and consequently a mismatch of the decoding pattern. In fact, SEM images recorded after the experiment revealed a strong contamination of the illuminated areas, i.e., the object and reference apertures, probably with

carbon which is a typical deposit on optical elements for high-intensity x-ray illumination due to cracking of residual gas contaminants. While such contaminations play a minor role at the Co *L*-edge, where the transmission through carbon is high, its effect is much stronger for photons of lower energy at the Co *M*-edges. Such a contamination may increase the resolution of a single pinhole by reducing its diameter. On the other hand, for each individual pinhole of an URA the contamination may affect the size and shape somewhat differently, distorting the homogeneity of the array and, thus, resulting in an overall adverse effect. In that case the single reference image would profit from the contamination whereas the mURA image would not. Again, a possible way to increase the spatial resolution for the mURA image in the future might be to use the measured pinhole image of the mURA to quantify the at-wavelength transmission of each single aperture and use this information as input for further iterative refinement.

The SNR ratio of mURA and pinhole is 1.2 for the one accumulation time recorded, i.e., a slight advantage for mURA imaging over use of a single pinhole as a reference structure is present in this high photon dose regime. We note that in comparison to the use of XMCD at the Co *L*-edge, the magnetic contrast *within* the object in the *M*-edge case is much weaker. Furthermore, the overall transmission through the entire object FOV is different as determined by the effective optical constants of such multilayer films. Especially in the XUV spectral range, the latter are not well known and further detailed analysis of the impact of the object contrast as

well as of the total intensity balance between object and reference wave and its impact on SNR in the reconstructions will require additional investigations.

4. Conclusion

In conclusion, we have demonstrated the first use of a modified URA for resonant spectro-holographic imaging at XUV and soft x-ray wavelengths. We are able to image ferromagnetic domain patterns at both the L_3 and $M_{2,3}$ absorption edges of Co and directly compare them with a respective hologram recorded under identical conditions via a single pinhole reference. At the Co L-edge the domain structure is reproduced within the spatial resolution of 50 nm. At the Co M-edges we estimate a spatial resolution of about 90 nm from the pinhole/mURA cross cor-relation. In contrast, the single pinhole can resolve smaller domain features of about 65 nm, in agreement with the nominal diameter of the reference aperture. The loss of spatial resolution is attributed to inhomogeneities of the mURA, possibly caused by contamination. We analyze the gain in signal-to-noise in the reconstructed real-space magnetization map obtained by using the mURA versus single pinhole reference as a function of incident photon dose and comparing single helicity and helicity difference holograms. In the low-exposure limit, a 2.5-fold increase in the SNR for a given exposure is observed for dif-ference helicity holograms, which is in line with theoretical expectations. For single helicity holograms, we see a 1.5-fold SNR increase. We speculate that this difference is due to the cancelation of systematic artifacts scaling with the dose in the difference helicity case, but in-depth simulations will be required to clarify this point. For increasing exposure time of the holograms, the relative SNR advantage of the mURA over a single pinhole decreases. Artifacts from imperfect mURA manufacturing and, thus, imperfect matching of the decoding pattern can be expected as the origin of this decreasing benefit. We have used the at-wavelength transmission of the mURA which is encoded via the additional single pinhole reference in the multiplexed hologram so far only to determine mURA pitch and orientation; the additional use of the mURA transmission in each of its apertures will allow higher order corrections in mURA-based imaging in the future. The signal-to-noise benefit of mURA based (soft) x-ray holography will obviously be decisive in limited photon number situations, such as encoun-tered for single-shot imaging, e.g., at free-electron x-ray laser sources and at laboratory sources such as when pushing towards either shorter wavelength or sub-fs temporal resolution.

Acknowledgments

References

[1] Pfau B and Eisebitt S 2016 X-ray holography *Synchrotron Light Sources and Free-Electron Lasers* ed E J Jaeschke *et al* (Berlin: Springer) pp 1093–133

[2] Eisebitt S, Lüning J, Schlotter W F, Lörgen M, Hellwig O, Eberhardt W and Stöhr J 2004 *Nature* **432** 885–8

[3] Stadler L-M, Gutt C, Autenrieth T, Leupold O, Rehbein S, Chushkin Y and Grübel G 2008 Hard X ray holographic diffraction imaging *Phys. Rev. Lett.* **100** 245503

[4] Wang T *et al* 2012 Femtosecond single-shot imaging of nanoscale ferromagnetic order in Co/Pd multilayers using resonant x-ray holography *Phys. Rev. Lett.* **108** 267403

[5] Pfau B *et al* 2010 Femtosecond pulse x-ray imaging with a large field of view *New J. Phys.* **12** 095006

[6] Rosenhahn A, Barth R, Cao X, Schürmann M, Grunze M and Eisebitt S 2007 Vacuum-ultraviolet Gabor holography with synchrotron radiation *Ultramicroscopy* **107** 1171–7

[7] Mancuso A P *et al* 2010 Coherent imaging of biological samples with femtosecond pulses at the free-electron laser FLASH *New J. Phys.* **12** 035003

[8] von Korff Schmising C *et al* 2014 Imaging ultrafast demagnetization dynamics after a spatially localized optical excitation *Phys. Rev. Lett.* **112** 217203

[9] Tao Z, Chen C, Szilvási T, Keller M, Mavrikakis M, Kapteyn H and Murnane M 2016 Direct time-domain observation of attosecond final-state lifetimes in photoemission from solids *Science* **353** 62–7

[10] Popmintchev D *et al* 2015 Ultraviolet surprise: efficient soft x-ray high-harmonic generation in multiply ionized plasmas *Science* **350** 1225–31

[11] Monserud N C, Malm E B, Wachulak P W, Putkaradze V, Balakrishnan G, Chao W, Anderson E, Carlton D and Marconi M C 2014 Recording oscillations of sub-micron size cantilevers by extreme ultraviolet Fourier transform holography *Opt. Express* **22** 4161–7

[12] Malm E B, Monserud N C, Brown C G, Wachulak P W, Xu H, Balakrishnan G, Chao W, Anderson E and Marconi M C 2013 Tabletop single-shot extreme ultraviolet Fourier transform holography of an extended object *Opt Express* **21** 9959–66

[13] Sandberg R L, Raymondson D A, La-o-vorakiat C, Paul A, Raines K S, Miao J, Murnane M M, Kapteyn H C and Schlotter W F 2009 Tabletop soft-x-ray Fourier transform holography with 50 nm resolution *Opt. Lett.* **34** 1618–20

[14] Sandberg R L *et al* 2008 High numerical aperture tabletop soft x-ray diffraction microscopy with 70 nm resolution *Proc. Natl Acad. Sci.* **105** 24–7

[15] Günther C M, Radu F, Menzel A, Eisebitt S, Schlotter W F, Rick R, Lüning J and Hellwig O 2008 Steplike versus continuous domain propagation in Co/Pd multilayer films *Appl. Phys. Lett.* **93** 072505

[16] Günther C M *et al* 2010 Microscopic reversal behavior of magnetically capped nanospheres *Phys. Rev.* B **81** 064411

[17] Pfau B *et al* 2011 Origin of magnetic switching field distribution in bit patterned media based on pre-patterned substrates *Appl. Phys. Lett.* **99** 062502

[18] Pfau B, Günther C M, Guehrs E, Hauet T, Hennen T, Eisebitt S and Hellwig O 2014 Influence of stray fields on the switching-field distribution for bit-patterned media based on pre-patterned substrates *Appl. Phys. Lett.* **105** 132407

[19] Hauet T, Günther C M, Pfau B, Schabes M E, Thiele J-U, Rick R L, Fischer P, Eisebitt S and Hellwig O 2008 Direct observation of field and temperature induced domain replication in dipolar coupled perpendicular anisotropy films *Phys. Rev.* B **77** 184421

[20] Büttner F *et al* 2015 Dynamics and inertia of skyrmionic spin structures *Nat. Phys.* **11** 225–8

[21] Schlotter W F *et al* 2006 Multiple reference Fourier transform holography with soft x rays *Appl. Phys. Lett.* **89** 163112

[22] Martin A V *et al* 2014 X-ray holography with a customizable reference *Nat. Commun.* **5** 4661

[23] Marchesini S *et al* 2008 *Nat. Photon.* **2** 560–3

[24] Geilhufe J *et al* 2014 Monolithic focused reference beam x-ray holography *Nat. Commun.* **5** 3008

[25] Fenimore E E and Cannon T M 1978 Coded aperture imaging with uniformly redundant arrays *Appl. Opt.* **17** 337–47

[26] Gottesman S R and Fenimore E E 1989 New family of binary arrays for coded aperture imaging *Appl. Opt.* **28** 4344–52

[27] Eisebitt S, Lörgen M, Eberhardt W, Lüning J, Stöhr J, Rettner C T, Hellwig O, Fullerton E E and Denbeaux G 2003 Polarization effects in coherent scattering from magnetic specimen: implications for x-ray holography, lensless imaging, and correlation spectroscopy *Phys. Rev. B* **68** 104419

[28] Willems F, Smeenk C T L, Zhavoronkov N, Kornilov O, Radu I, Schmidbauer M, Hanke M, von Korff Schmising C, Vrakking M J J and Eisebitt S 2015 Probing ultrafast spin dynamics with high-harmonic magnetic circular dichroism spectroscopy *Phys. Rev. B* **92** 220405

[29] Büttner F, Schneider M, Günther C M, Vaz C A F, Lägel B, Berger D, Selve S, Kläui M and Eisebitt S 2013 Automatable sample fabrication process for pump-probe x-ray holographic imaging *Opt. Express* **21** 30563–72

[30] Valencia S, Gaupp A, Gudat W, Mertins H-C, Oppeneer P M, Abramsohn D and Schneider C M 2006 Faraday rotation spectra at shallow core levels: 3p edges of Fe, Co, and Ni *New J. Phys.* **8** 254

[31] Chen C T, Idzerda Y U, Lin H-J, Smith N V, Meigs G, Chaban E, Ho G H, Pellegrin E and Sette F 1995 Experimental confirmation of the x-ray magnetic circular dichroism sum rules for iron and cobalt *Phys. Rev. Lett.* **75** 152–5

[32] Hellwig O, Berger A, Kortright J B and Fullerton E E 2007 Domain structure and magnetization reversal of antiferromagnetically coupled perpendicular anisotropy films *J. Magn. Magn. Mater.* **319** 13–55

[33] The parameters of the BESSY-II beamlines are tabulated at http://helmholtz-berlin.de/user/experimental-infrastructures/instruments-photons/bessy-beamline_en.html (accessed 21 November 2016)

[34] Flewett S, Günther C M, von Korff Schmising C, Pfau B, Mohanty J, Büttner F, Riemeier M, Hantschmann M, Kläui M and Eisebitt S 2012 Holographically aided iterative phase retrieval *Opt. Express* **20** 29210–6

[35] Schaffert S, Pfau B, Geilhufe J, Günther C M, Schneider M, von Korff Schmising C and Eisebitt S 2013 *New J. Phys.* **15** 093042

[36] Kortright J B, Kim S-K, Denbeaux G P, Zeltzer G, Takano K and Fullerton E E 2001 Soft-x-ray small-angle scattering as a sensitive probe of magnetic and charge heterogeneity *Phys. Rev. B* **64** 092401

[37] Hellwig O, Denbeaux G P, Kortright J B and Fullerton E E 2003 X-ray studies of aligned magnetic stripe domains in perpendicular multilayers *Physica* B **336** 136–44

[38] Nugent K 1991 Signal to noise ratio in soft x-ray holography *J. Mod. Opt.* **38** 553–63

[39] Chapman H N *et al* 2006 Femtosecond diffractive imaging with a soft-x-ray free-electron laser *Nat. Phys.* **2** 839–43